Impurity-induced pairing in two-dimensional Fermi gases

Ruipeng Li,[1, 2, *] Jonas von Milczewski,[1, 2, *] Atac Imamoglu,[3] Rafał Ołdziejewski,[1, 2] and Richard Schmidt[1, 4]

[1]*Max-Planck-Institute of Quantum Optics, Hans-Kopfermann-Strasse 1 , 85748 Garching, Germany*
[2]*Munich Center for Quantum Science and Technology (MCQST), Schellingstr. 4, 80799 Munich, Germany*
[3]*Institute of Quantum Electronics ETH Zurich, CH-8093 Zurich, Switzerland*
[4]*Institute for Theoretical Physics, Heidelberg University, Philosophenweg 16, 69120 Heidelberg, Germany*

(Dated: November 23, 2022)

We study induced pairing between two identical fermions mediated by an attractively interacting quantum impurity in two-dimensional systems. Based on a Stochastic Variational Method (SVM), we investigate the influence of confinement and finite interaction range effects on the mass ratio beyond which the ground state of the quantum three-body problem undergoes a transition from a composite bosonic trimer to an unbound dimer-fermion state. We find that confinement as well as a finite interaction range can greatly enhance trimer stability, bringing it within reach of experimental implementations such as found in ultracold atom systems. In the context of solid-state physics our solution of the confined three-body problem shows that exciton-mediated interactions can become so dominant that they can even overcome detrimental Coulomb repulsion between electrons in atomically-thin semiconductors. Our work thus paves the way towards a universal understanding of boson-induced pairing across various fermionic systems at finite density, and opens perspectives towards realizing novel forms of electron pairing beyond the conventional paradigm of Cooper pair formation.

I. INTRODUCTION

Frequently, the relevant physics of a many-body system is determined by the properties of its few-particle correlators, and thus a deep understanding of a many-body problem often comes only after carefully examining its few-body counterpart. An excellent example is given by the discovery of Cooper pair formation as the key ingredient leading to superconductivity [1, 2]. No matter the type of a superconductor, be it s-wave, p-wave, d-wave or other like charge-$4e$ superconductors [3–12], the phenomenon requires electrons to be bound into bosonic compounds. While, for conventional superconductors, the binding originates from phonon-mediated attraction, a variety of bosons —partially originating from collective excitations of the electronic system itself— have been considered as the mediating particle [13–16].

More generally, quantum impurity-mediated pairing of fermions in the so-called mass-imbalanced $1 + N$ fermions problem has been scrutinized extensively in recent years [17–28]. The vast majority of theoretical efforts have focused on non-interacting fermions and point-like impurity-fermion attraction that can be studied experimentally with ultracold gases [29–31]. Interestingly, in the unconfined case, the system easily supports cluster-bound states whenever fermions are sufficiently heavier than the quantum impurity. The mass ratios required for a specific cluster creation depend on the dimensionality of the system, being more favourable (smaller) in two dimensions (2D) compared to three dimensions (3D) [32, 33].

A recent twist to the quantum impurity problem in 2D emerged with the advent of atomically-thin van der Waals materials, particularly semiconducting transition metal dichalcogenides (TMDs) [34, 35]. In TMDs, excitons (bosons) can be either employed as an experimental probe of the many-body physics exhibited by electrons (fermions), ranging from Mott physics [36], excitonic insulators [37] and the fractional Quantum Hall effect [38] to the recent observation of Wigner crystallisation [39, 40], or they can be viewed as novel constituents of Bose-Fermi mixtures [34, 41, 42] potentially supporting superconductivity [43–45]. Importantly, in this case strong Coulomb repulsion is present between the fermionic electrons and the impurity-fermion interaction itself is characterized by a substantial range [46]. So far, little is known about the existence and character of bosonic cluster-bound states in such a scenario.

Recent advances in controlling 2D external confinement in ultracold setups [47, 48] and TMDs [49] open an exciting possibility of exploring the physics of the quantum impurity problem in a fermionic background in a controlled bottom-up approach [50–52]. Specifically, an alternative interpretation of the confinement potential is that of imitating a finite bath density found in many-body problems like the Fermi polaron problem [53–56]. As such, the change of the confinement ($\sim R$, see Fig. 1) could be regarded as a primitive means of tuning the bath density ($n_F \sim 1/R^2 \sim k_F^2$), realising a few-body analogue of the full many-body problem.

In this work, we significantly refine the previous understanding of a 2D system of one impurity and two identical fermions (i.e., the smallest possible Fermi sea) by studying the effects of a finite-range impurity-fermion potential, confinement and strong inter-fermion repulsion on the ground state properties using a Stochastic Variational Method (SVM). As a key result, we show that the
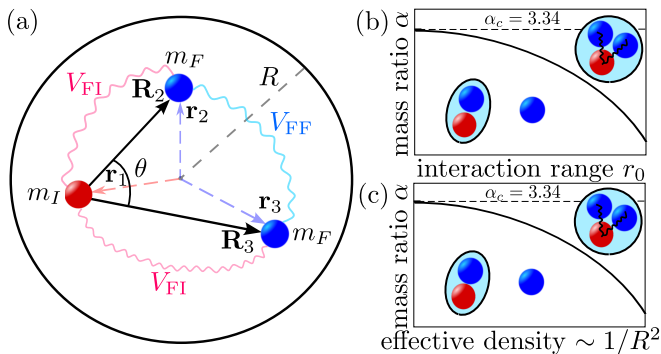
arXiv:2211.12495v1 [cond-mat.quant-gas] 22 Nov 2022

FIG. 1. Schematic diagram of the system and the main effects under study. Panel (a) shows the interacting three-body system with one impurity ("I") and two fermions ("F") in a two-dimensional spherical box of size R. On the right, we show the qualitative effect of (b) the interaction range r_0 and (c) the effective density (inversely proportional to the inverse of the box size R) on the critical mass ratio of the dimer-trimer transition. Both interaction range and effective density enhance trimer formation and can become so dominant that they can even overcome the detrimental Coulomb repulsion (V_{FF}) between the fermions.

critical mass ratio of the dimer-to-trimer transition (in a TMD signified as the transition from a fermionic trion to a bosonic p-wave bound state of two electrons glued together by an exciton) strongly departs from previous findings obtained for the simpler case of ideal fermions and zero-range impurity-fermion attraction. Remarkably, for TMDs, we find that the trimer formation, comprising two identical electrons and an exciton, is robust against Coulomb repulsion for a vast range of parameters. Moreover, we find that the stability of emerging bosonic p-wave composite electronic state is enhanced by confinement suggesting that direct exciton-mediated p-wave superconductivity may be well in reach in solid state systems.

II. THE MODEL

We consider an interacting system of two fermions and a quantum impurity confined in a two-dimensional spherical box, see Fig. 1a. This could represent two electrons interacting with an exciton in a quantum dot within a TMD, as well as two degenerate ultracold fermionic atoms interacting with an atom of a different quantum number within an oblate optical trap. Using an effective mass approximation, the Hamiltonian for this system reads

$$
H = -\frac{\hbar^2}{2m_I}\nabla_1^2 - \frac{\hbar^2}{2m_F}\nabla_2^2 - \frac{\hbar^2}{2m_F}\nabla_3^2 + \sum_{i=1}^{3} V_{\text{conf}}(\mathbf{r}_i)
$$
$$
+ V_{\text{FI}}(\mathbf{r}_1 - \mathbf{r}_2) + V_{\text{FI}}(\mathbf{r}_1 - \mathbf{r}_3) + V_{\text{FF}}(\mathbf{r}_2 - \mathbf{r}_3).
$$
(1)

Here $\mathbf{r}_1$, $\mathbf{r}_2$ and $\mathbf{r}_3$ denote the positions of the impurity and the two fermions, respectively, while m_I and m_F are their masses. The fourth term in the Hamiltonian represents the external confinement potential which is modeled by an infinite potential well [57]. To account for finite range effects the fermion-impurity interaction is modeled via a square well potential

$$
V_{\text{FI}}(\mathbf{r}) = \begin{cases} -V_0, & |\mathbf{r}| \leq r_0 \\ 0, & |\mathbf{r}| > r_0 \end{cases},
$$
(2)

of depth V_0 and range r_0. Additionally, to study the influence of Coulomb interactions, we include the simple Coulomb potential

$$
V_{\text{FF}}(\mathbf{r}) = \frac{e^2}{4\pi\epsilon_0\epsilon}\frac{1}{|\mathbf{r}|},
$$
(3)

where e is the electron charge and ϵ the dielectric constant of a given material. Note that in cold atoms this direct interaction is absent ($V_{\text{FF}} = 0$) while for TMD it is a good approximation at large distance scales. At short range this interaction can be modelled using the Rytova-Keldysh potential [58, 59]. However, to capture the essential physics of the interplay of Coulomb repulsion, confinement and electron-exciton attraction, we restrict ourselves to the use of the pure Coulomb potential (3) which, on the one hand, allows for efficient numerics and, on the other hand, does not complicate the analysis by introducing additional physical tuning parameters, such as the screening length.

III. METHOD

Apart from the task of solving the quantum mechanical problem of three interacting particles, this system brings with itself the challenge of the additional confinement potential which is however crucial to imitate the effect of a finite fermion density n_F in many-body systems, $n_F \sim 1/R^2 \sim k_F^2$ where k_F denotes the Fermi wavevector of the fermions. The confinement breaks translational symmetry and thus is not susceptible to momentum space approaches using conventional variational wave functions or quantum field theory and diagrammatic approaches.

To solve for the ground state and its energy, we employ the SVM [60]. To this end, the Hamiltonian H is diagonalized with respect to a set of wavefunctions $\{\Phi_n\}_{n=1}^{N}$ which is successively extended by drawing from a manifold of trial functions. In every extension step $N \to N+1$ the choice of the new wavefunction Φ_{N+1} is optimized in a stochastic random walk, minimizing the lowest-lying eigenstates of the Hamiltonian H with respect to the vector space spanned by the set $\{\Phi_n\}_{n=1}^{N+1}$. During the optimization, we first draw a set of independent samples from the manifold of trial functions and then perform a random descend walk around the best proposal state. Having performed an extension step, the Hamiltonian H is diagonalized with respect to the vector space spanned

by the $\{\Phi_n\}_{n=1}^{N+1}$. The resulting i-lowest eigenstate Ψ_i is then given by a superposition of these basis states, i.e. $\Psi_i = \sum_{n=1}^{N+1} c_n^i \Phi_n$, where $i = 1, ..., N + 1$ and the eigenstates $\{\Psi_i\}_{i=1}^{N+1}$ are mutually orthogonal.

In many applications of SVM, trial functions are generated from explicitly correlated Gaussians (ECG)[60, 61]. These are parametrized as $\Phi(\mathbf{r}_1, \mathbf{r}_2, \mathbf{r}_3) = \mathcal{P} \exp\left(-\frac{1}{2} \sum_{i,j=1}^{3} A_{ij} \mathbf{r}_i \cdot \mathbf{r}_j\right)$, where A is a positive definite, symmetric 3×3 matrix and $\mathcal{P}$ is an antisymmetrization operator. The advantage of using this trial function is threefold. First, it is easy to find the analytical solution to the matrix elements of the Hamiltonian with these basis functions [61, 62]. Second, it can achieve a high accuracy in the energy. Finally, the ECG contain the relevant physical states (dimers, trimers and scattering states in our system) and as such have been used to calculate exciton, trion and even biexciton energies in solid state systems with high precision [63–66]. For more detail on the optimization algorithm and the sampling from the ECG manifold, we refer to Appendix A.

IV. GROUND STATE

In this section, we calculate the ground state using the SVM. As the 2D system features binding via the fermion-impurity potential V_{FI} for any potential depth [67], states composed of a dimer and a further fermion in a scattering state are expected to play a vital role [68]. Moreover, for sufficiently light impurities the formation of a trimer is expected in which two fermions and the impurity bind together by the mediating force of the impurity [28]; similar to the three-dimensional case where a p-wave trimer and eventually Efimov states appear for sufficiently light impurities [17, 19, 21]. In the limit of a vanishing interaction range $r_0 \to 0$ and infinite system size $R \to \infty$ a ground state transition from a dimer to a trimer state is predicted to occur as the mass ratio $\alpha = m_F/m_I$ is tuned across the critical value $\alpha_c \approx 3.34$ [23, 32, 33]. Having this known, limiting case of the system under study as a benchmark, in the following we investigate the effect of interaction range r_0 and confinement (determined by the system size R) on the position of this transition, which manifests as a crossover in our system of a finite size. Specifically, we study how the ground state characteristics and energy changes as we tune α, r_0 and R and as a result how the critical mass ratio varies with r_0 and R. In the following, we will refer to the two-body bound state appearing in a two-body problem consisting of the impurity and a fermion as the *vacuum dimer* and its binding energy as the *vacuum dimer energy* E_{2B}^∞. The terms *dimer* and *trimer* will refer to states in the three-body problem, where the term *dimer* refers to a two-body bound state of an impurity and a fermion along with a fermion in a scattering state, while the term *trimer* denotes a three-body bound state consisting of an impurity bound to the two fermions.

To this end, we vary α, r_0 and R while keeping the non-trapped ($R \to \infty$) vacuum dimer energy E_{2B}^∞ constant and operate in units where the fermion mass is set to $m_F = 0.5$. We define a corresponding length scale $r_B = 1/\sqrt{2m_F E_{2B}^\infty}$, which we will refer to as binding length in the following. Note, however, that we set this length by the fermion mass and not the reduced mass in order to have a fixed value of r_B as α is changed and thus it is merely proportional to the physical interpretation of a binding length. The required solution for the ground state of the two-body Hamiltonian of one fermion and one impurity interacting via V_{FI} for $R \to \infty$ can be obtained exactly (see Appendix B; in Appendix C we show for comparison the vacuum dimer energies obtained for $R < \infty$ using the SVM). From this solution the potential depth V_0 is obtained as a function of α and r_0. We begin by considering the system without Coulomb interactions ($V_{\text{FF}} = 0$). Thus, after establishing the trimer formation in our system, we will turn to studying the effect of Coulomb interactions ($V_{\text{FF}} > 0$).

A. Non-interacting fermions

In Fig. 2, we show the energy of the SVM ground state as function of the mass ratio α for different r_0 and R. Here, r_0 and R are varied in terms of the dimensionless quantities r_0/r_B and R/r_B. The ground state energies are all located in vicinity of E_{2B}^∞. For fixed r_0/r_B and R/r_B, the ground state energies first increase slightly with the mass ratio and then show a drop at some critical mass ratio. Beyond the critical mass ratio, the ground state energy decreases steadily and takes on an almost linear dependence on the mass ratio $E \propto -\alpha$ [23, 32, 33]. One can see that r_0 and R have a strong influence on the energies as well as the critical mass ratio at which the qualitative change in the ground state energy, represented by the drop, occurs. For a fixed system size R/r_B, upon increasing r_0/r_B, both the ground state energies and the critical mass ratio decrease. On the other hand, fixing the interaction range r_0/r_B while increasing system size R leads to a decrease of the energy while the critical mass ratios increases.

We now turn to a detailed discussion of the qualitative change observed in the ground state energy. This change signifies a transition of the ground state of the system, where for values of α smaller than a critical value, the system is composed of a bound dimer plus an unbound fermion. In contrast, beyond the critical value of α the ground state energy falls below the corresponding dimer-fermion scattering threshold signifying the emergence of a three-body bound state, the trimer, similar to the unconfined system [23, 32, 33]. While the energy is a good indicator of a qualitative change, a reliable identification of the nature of the ground state, can be obtained by a direct analysis of the corresponding wave function. In the following, we will study two measures, angular momentum and density distribution, from which the dimer
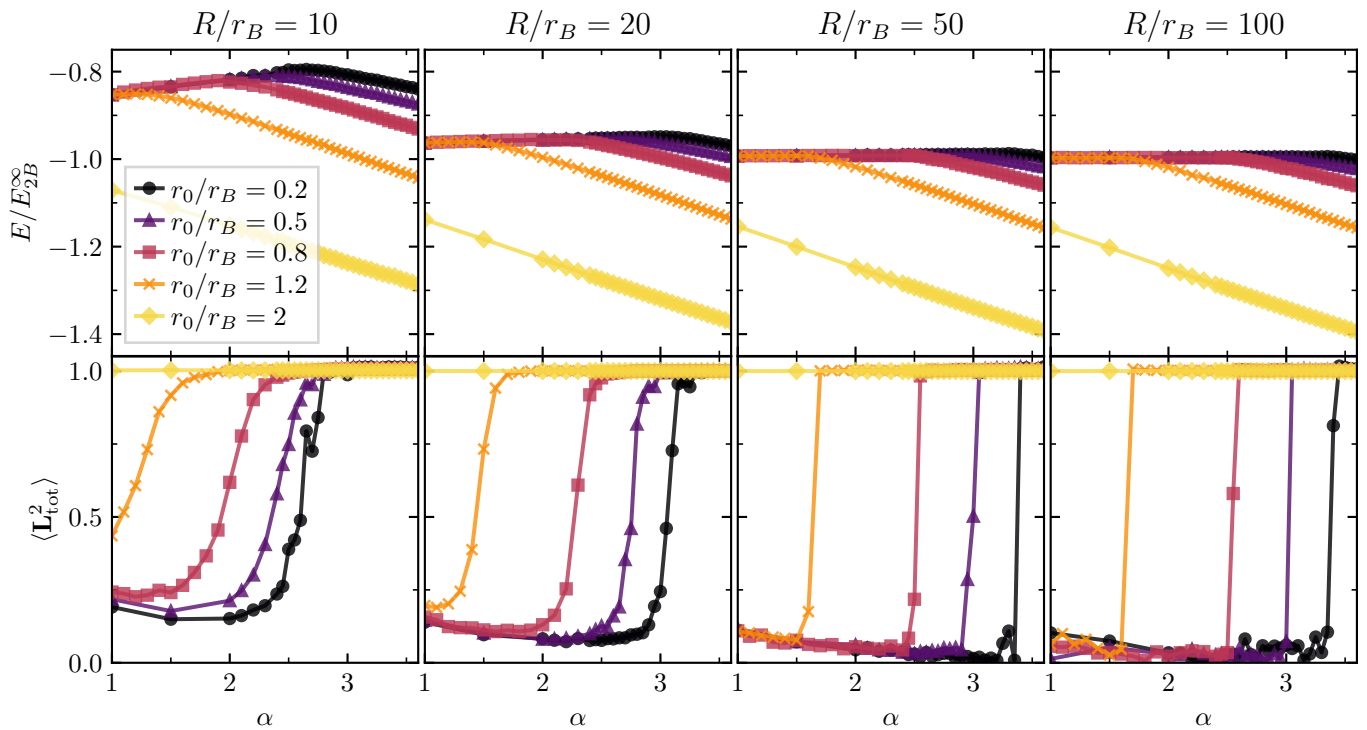
FIG. 2. Energies E/E_{2B}^∞ (top panels) and angular momentum expectation values $\langle \mathbf{L}_{\text{tot}}^2 \rangle$ (bottom panels) of the ground state as a function of mass imbalance α for $r_0/r_B = 0.2$ (black dots), 0.5 (purple triangles), 0.8 (red squares), 1.2 (orange crosses) and 2 (yellow diamonds) at $R/r_B = 10$, 20, 50 and 100. The energies are located around E_{2B}^∞ with upward shifts mainly due to the confinement contributions to the kinetic energy of the particles, and additional contributions due to the interaction range. The crossover from the dimer to the p-wave trimer bound state is clearly visible in the angular momentum which crosses over from close to 0 to approximately 1. This crossover is similarly reflected in a drop of the ground state energy that turns into an almost linear dependence on α beyond a critical value. For increasing r_0/r_B (R/r_B) this crossover region moves to lower (higher) mass ratios α. For $R/r_B \to \infty$ the crossover becomes a sharp transition which for $r_0/r_B \to 0$ occurs at $\alpha_c \approx 3.34$ [23, 32, 33]; remnants of this are visible for $R/r_B = 100$.

and trimer states can be clearly distinguished.

First we focus on the analysis of angular momentum (see lower column of Fig. 2). Here we introduce the relative coordinates $\mathbf{R}_2 = \mathbf{r}_2 - \mathbf{r}_1$ and $\mathbf{R}_3 = \mathbf{r}_3 - \mathbf{r}_1$ where $\mathbf{R}_2$ and $\mathbf{R}_3$ denote the positions of the fermions relative to the impurity. The total angular momentum relative to the impurity particle is then given by $\mathbf{L}_{\text{tot}} = \mathbf{L}_2 + \mathbf{L}_3$ where $\mathbf{L}_2 = \mathbf{R}_2 \times \mathbf{P}_2$ and $\mathbf{L}_3 = \mathbf{R}_3 \times \mathbf{P}_3$, with $\mathbf{P}_2$ and $\mathbf{P}_3$ the momentum operators of $\mathbf{R}_2$ and $\mathbf{R}_3$, respectively. In this frame, due to the fermionic statistics, the trimer has to have odd, finite angular momentum $\langle \mathbf{L}_{\text{tot}} \rangle = \pm 1$, while the dimer state has $\langle \mathbf{L}_{\text{tot}} \rangle = 0$ [23, 28, 32, 33, 69].

However, as a result of the ECG functions we use, the basis functions are real and hence any measured value of $\langle \mathbf{L}_{\text{tot}} \rangle$ has to vanish. Thus the ground state wavefunction of a trimer state obtained from the SVM is an equal superposition of degenerate ground states with $\langle \mathbf{L}_{\text{tot}} \rangle = 1$ and $\langle \mathbf{L}_{\text{tot}} \rangle = -1$; resulting in the expectation value $\langle \mathbf{L}_{\text{tot}} \rangle = 0$. For this reason, we consider the expectation value $\langle \mathbf{L}_{\text{tot}}^2 \rangle$ which allows us to distinguish the dimer and trimer state (for more details, we refer to Appendix D).

In the lower column of Fig. 2 we show the value of $\langle \mathbf{L}_{\text{tot}}^2 \rangle$ of the ground state. As one can see, $\langle \mathbf{L}_{\text{tot}}^2 \rangle$ sharply

increases from values close to 0 to approximately 1 as the mass ratio is varied beyond a critical value. The region in which this qualitative change occurs coincides with the critical mass ratio at which the drop in energy is observed. Akin to the behavior of energy, tuning r_0/r_B and R/r_B the crossover region moves in the same direction. While for smaller system sizes the transition region is larger, with increasing system size the transition region becomes more narrow, indicating that the crossover found for a finite system turns into a sharp transition for an infinite system size.

From the behavior of energy and angular momentum a simple physical picture of the crossover from a dimer to a trimer arises. At small mass ratios α, the ground state is given by a dimer along with a fermion in a delocalized scattering state. Thus for large system sizes, the energy approaches the two-body energy E_{2B}^∞. However, for smaller system sizes the confinement induces exchange-, correlation- and confinement-energies between the two fermions increasing the energy above E_{2B}^∞. This increase in energy is larger for smaller system sizes, and features an additional weak dependence on mass ratio which can be understood already from the non-interacting sys-
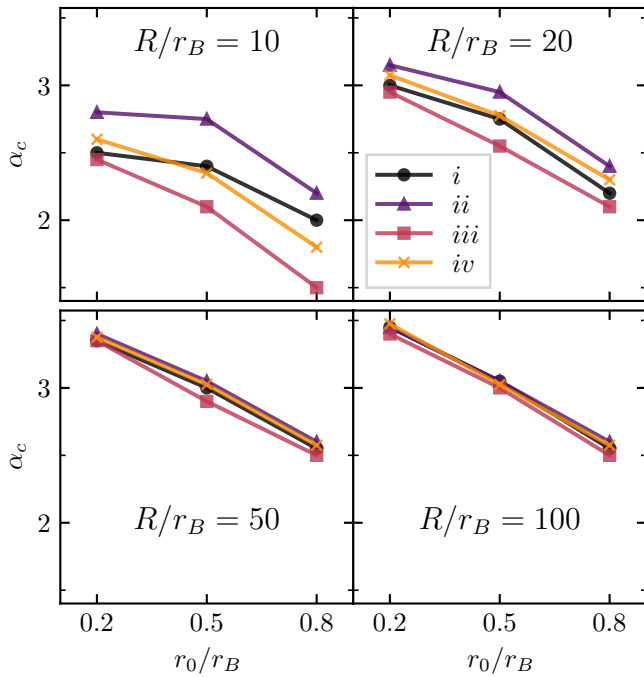
FIG. 3. Critical mass ratio for the dimer to trimer transition as function of the interaction range r_0/r_B for $R/r_B = 10, 20, 50, 100$ determined using different criteria. The criteria are: i. energy drop (black dots); ii. $\langle \mathbf{L}_{\text{tot}}^2 \rangle \approx 1$ (purple triangles); iii. $\langle \mathbf{L}_{\text{tot}}^2 \rangle \approx 0$ (red squares); iv. $\langle \mathbf{L}_{\text{tot}}^2 \rangle \approx 0.5$ (yellow crosses). As described in the main text, the critical mass ratio increases with R/r_B and decreases with r_0/r_B. The different criteria obtain different values with the $\langle \mathbf{L}_{\text{tot}}^2 \rangle \approx 0$ criterion consistently giving the lowest mass ratio and the $\langle \mathbf{L}_{\text{tot}}^2 \rangle \approx 1$ criterion giving the highest. With increasing R/r_B the crossover region becomes narrower which also decreases the dispersion of the different methods.

tem where the confinement energy is given by $E_{\text{conf}} = z_{01}^2/2m_I R^2 + z_{11}^2/m_F R^2 = (z_{01}^2\alpha/2 + z_{11}^2)/m_F R^2$ with z_{01} and z_{11} the first zero of the Bessel functions J_0 and J_1. Beyond a critical mass ratio, the ground state is described by a trimer state and its energy starts to decrease close to linearly with mass ratio, as also obtained in the continuum case [23, 32, 33].

We now turn to a more detailed analysis how the system size R and interaction range r_0 affect the critical mass ratio α_c (see Fig. 3). Decreasing the system size has a stronger effect on the dimer state than on the trimer state as the unbound fermion in its delocalized scattering state feels the confinement stronger than a fermion bound tightly to the impurity. Thus the trimer state is subject to a confinement energy contribution less than the dimer state. Consequently, decreasing system size moves the transition to smaller mass ratios.

Conversely, increasing the interaction range r_0 affects the trimer state stronger than it affects the dimer state because for $R \gg r_0$ the average distance between the fermions in a trimer state is related to the short distance scales r_B and r_0 while in the dimer state (including the
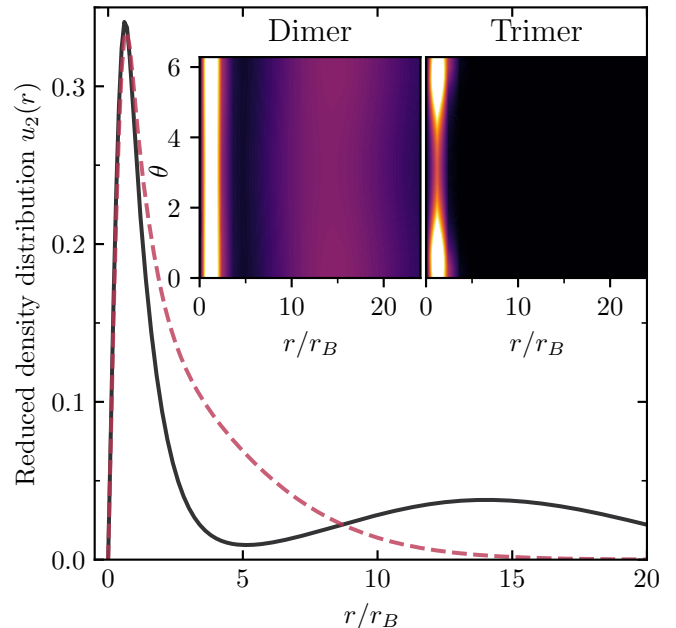

FIG. 4. Reduced density distributions of a dimer ($\alpha = 2$) and trimer ($\alpha = 3$) state. The plot shows $u_2(r)$ for a dimer (black, solid) and a trimer (red, dashed) state for $R/r_B = 20$ and $r_0/r_B = 0.8$. The exponential decay of the trimer distribution is clearly visible while the dimer holds a fermion that is delocalized at the length scale of the system size. The inset shows $u_1(r, \theta)$ for the trimer (left) and the dimer state (right). The exponential decay and the delocalized tail, respectively, are visible and in both cases a slight tendency towards antiparallel orientation of the fermions is present.

unbound fermion) it is related to R. Thus, increasing r_0 lowers the Pauli-repulsion within the trimer state, making the trimer favorable and lowering the critical mass ratio. This intuitive picture is reflected in the numerical results presented in Fig. 3. In this Figure, we additionally analyse the increasing sharpness of the transition as the system size is increased by showing the critical mass ratio as obtained from different criteria imposed on the energy and the angular momentum. As one can see for $R/r_B = 100$ all criteria give nearly identical results and only a dependence on the scale r_0 remains.

As can be seen from the lower panel in Fig. 2, the impact of the interaction range and system size on the dimer and trimer state is also reflected in the angular momentum. Due to the confinement, the free fermion in the dimer state is forced to take on a finite angular momentum state, resulting in a nonzero value of $\langle \mathbf{L}_{\text{tot}}^2 \rangle$. As the system size is increased, the free fermion is less affected and $\langle \mathbf{L}_{\text{tot}}^2 \rangle$ approaches zero. The trimer, on the other hand, is hardly affected by the finite system size as long as $R \gg r_0$ and thus $\langle \mathbf{L}_{\text{tot}}^2 \rangle$ is very close to 1. This behaviour shows that the critical mass ratio of 3.34 obtained in the limit $r_0 \to 0$, $R \to \infty$ [23, 32, 33], potentially features only a small window of universality because it has a strong dependence on r_0 and R. We note, that the critical

mass ratios in Fig. 3 for $R/r_B = 100$, $r_0/r_B = 0.2$ tend to lie slightly higher than the asymptotic value of 3.34. This is most likely due to the stochastic nature of our method in which, close to the transition, the energetic difference between dimer and trimer particles becomes small. As a result, especially for larger system size and shorter interaction range, a suitable trimer wavefunction can only be found for a high number of proposed wave functions. In Appendix A, we describe the used sampling method which speeds up this process by finding trimer wavefunctions more efficiently.

To further confirm the presence of two- and three-body bound states via the spatial localization of the fermions —or the lack thereof — around the impurity, we study the spatial structure of the ground state wavefunction. To this end, we consider the reduced density distribution, for in the trimer state the two fermions are both close to the impurity while in the dimer state one fermion is close to the impurity and the other is in a scattering state. Given the three-body wavefunction Ψ, we define the functions $u_1(r)$ and $u_2(r,\theta)$

$$u_1(r_2, \theta_2) = r_2 \int d^2\mathbf{r} d^2\mathbf{r_3} |\Psi(\mathbf{r}, \mathbf{r} + \mathbf{r_2}, \mathbf{r} + \mathbf{r_3})|^2, \quad (4)$$

$$u_2(r_2) = \int d\theta_2 u_1(r_2, \theta_2), \quad (5)$$

where $r_2 = |\mathbf{r_2}|$ and θ_2 denotes the angle with respect to $\mathbf{r_3}$. From this definition, one can see that the reduced density distribution u_1 is obtained by integrating out the coordinates of the impurity and of one of the fermions. Performing the additional integral over the angle θ_2 in the definition of u_1, one then obtains a measure of the probability of finding one fermion at a distance r_2 from the impurity. In Fig. 4, the density distributions are shown for exemplary trimer and dimer states. For the trimer state, the density distribution u_2 indeed exhibits an exponential decay in line with the expectation that both fermions are closely-bound to the impurity. In contrast, for the dimer state u_2 does not decay exponentially with r_2 but features a tail that corresponds to one of the fermions being situated in a scattering scattering state. The density plots of u_1 in the inset of Fig. 4 further illuminate this. They show that beyond the radial dependence, the fermions tend to slightly prefer anti-parallel configurations in the trimer state thus maximizing the inter-fermion distance within the bound state. For very short distances, the distributions approach 0 due to Pauli repulsion and the geometrical factor of r_2 in their distribution. For an additional analysis of the spatial structure of the ground states, we refer to Appendix E, where the reduced density distribution with respect to the radial dependencies after integrating out all angular coordinates is shown.
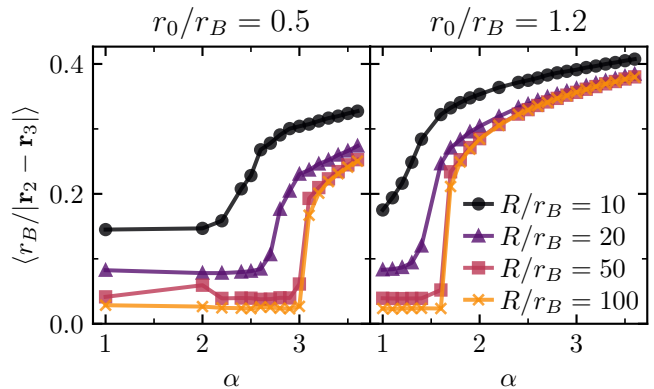

FIG. 5. Expectation value of $r_B/|\mathbf{r_2} - \mathbf{r_3}|$ of the ground state wavefunctions obtained in Section IV A, for $r_0/r_B = 0.5$ (left) and 1.2 (right) and $R/r_B = 10$ (black dots), 20 (purple triangles), 50 (red squares), 100 (orange crosses). The crossover from dimer to trimer state is visible in the expectation value. Increasing the box size R and decreasing the interaction range r_0 moves the crossover to higher α, consistent with our previous results. Moreover, the expectation values increase as the box size becomes smaller because the closer vicinity of the fermions results in a larger Coulomb energy.

B. Coulomb interaction

We now consider the impact a direct interaction between the two fermions ($V_{\text{FF}} > 0$) has on the dimer-trimer transition. In particular, we focus on Coulomb interactions present in 2D semiconductors (see Eq. (3)). In the trimer state, both electrons bind to the exciton bringing themselves closer together. Intuitively, this can give rise to a considerable increase in the total energy of the cluster. Consequently, if the Coulomb energy becomes larger than the energy gap between the trimer and dimer states, the ground state is thus expected to unbind into a dimer and free electron state.

To estimate roughly the impact of the Coulomb energy on the total energy, we first calculate the expectation value of the Coulomb interaction (up to constants) of the ground state of the system without Fermi-Fermi interaction, namely $\langle r_B/|\mathbf{r_2} - \mathbf{r_3}|\rangle$. We stress again (see Section II) that, in the following, we shall use the Coulomb potential instead of a more accurate approximation of 2D interactions between charges given by the Keldysh potential. In any case, since the Coulomb interaction is more extreme than the Keldysh potential at short range, we expect our choice to be more restrictive than the Keldysh interaction. In Fig. 5, the expectation value of $r_B/|\mathbf{r_2} - \mathbf{r_3}|$ is shown. We find a transition in the expectation value of $r_B/|\mathbf{r_2} - \mathbf{r_3}|$ while increasing the mass ratio. For dimer states, two electrons are relatively distant, rendering the value of $\langle r_B/|\mathbf{r_2} - \mathbf{r_3}|\rangle$ small. In contrast, for trimer states, this value is considerable and increases as the mass ratio rises. This simple estimation of the Coulomb energy in the trimer state already suggests the existence of a dimer-to-trimer transition even
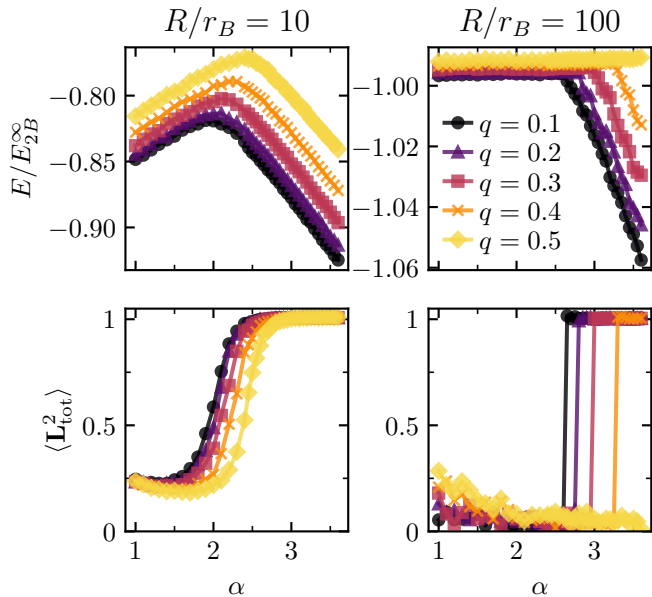
FIG. 6. Energies and expectation values of $\mathbf{L}_{\text{tot}}^2$ of the ground state of the system with Coulomb interaction with $r_0/r_B = 0.8$ and $R/r_B = 10$ (left) and 100 (right) for $q = 0.1$ (black dots), 0.2 (purple triangles), 0.3 (red squares), 0.4 (orange crosses), 0.5 (yellow diamonds). As in Fig. 2, the energy drop shows the crossover from a dimer to a trimer state which moves to higher α upon increasing the box size R and the effective charge q.

with non-zero Coulomb interaction.

Motivated by the above, we solve for the ground states of the system including the Coulomb interaction (3) by applying the SVM for different values of a dimensionless effective charge q defined by the square root of the ratio of Coulomb repulsion to dimer binding energy

$$q = \sqrt{\frac{V_{\text{FF}}(r_B)}{E_{2B}^\infty}} = \sqrt{\frac{2m_{\text{F}}r_B}{4\pi\epsilon_0\epsilon\hbar^2}}e. \qquad (6)$$

From the SVM, we calculate the energy and the expectation value of $\mathbf{L}_{\text{tot}}^2$ for an interaction range $r_0/r_B = 0.8$ and box sizes $R/r_B = 10$ and $R/r_B = 100$, see Fig. 6. Depending on the effective charge q, the energies drop for some critical mass ratio while the corresponding $\mathbf{L}_{\text{tot}}^2$ rapidly increase signaling a dimer-trimer crossover, similar to the case without Coulomb repulsion. The larger the effective charge q, the larger the critical value α_c becomes. Conversely, the larger the density n_F ($\sim 1/R^2 \sim k_F^2$), the smaller the critical value α_c which suffices for the dimer-to-trimer transition to occur. Notably, the dimer-to-trimer transition remains robust upon the strong, long-range Coulomb repulsion. While Coulomb interaction weakens trimer formation (increasing the critical value), it does not inhibit it as we have observed a transition to a trimer state for all effective charges we considered [70]. Simultaneously, one can off-

set the detrimental effects of Coulomb repulsion on forming a trimer by tighter confinement (i.e. larger effective electron density) or a larger interaction range.

Similar to Fig. 4, we show the reduced density distribution for the system with Fermi-Fermi interaction in Fig. 7. The effective charge and mass ratio were chosen to illustrate both dimer and trimer states as in Fig. 4. As can be seen, both states feature a localized part, while the dimer again exhibits the additional contribution of a delocalized scattering state. As before, a tendency towards anti-parallel fermion configuration in the trimer state can be seen. Increasing the effective charge q, the density distribution of the trimer decays at a larger length-scale showing clearly that the Fermi-Fermi repulsion tends to favor a larger Fermi-Fermi distance, while still accommodating for a trimer state. Similarly, on the dimer state this has the effect of moving the scattering tail away from the impurity-fermion bound state.

Experimentally, one could control the critical mass ratio α_c by tuning the effective electron charge, e.g. by changing a dielectric constant of the system [71]. For typical parameters and energy scales in TMDs, i.e. $\epsilon \approx 4.4$, $m_{\text{F}} \approx 0.5\,m_{\text{e}}$, where m_{e} indicates the bare electron mass, and $|E_{2B}^\infty| \approx 30$ meV (trion binding energy) [46], one arrives at $q \approx 2.6$. This value is consistent with the experimental observations of trions (corresponding to dimers in our work) as the ground state. While at first sight this might suggest the absence of the p-wave trimer state for typical TMD realizations, this estimate is obtained assuming a electronic system at vanishing density. In this regard, it is important to note that, as we also find, confinement naturally decreases the role of Coulomb interaction. In turn, regarding the increase in confinement as an increase in the effective electron density, our results suggest that at sufficiently high fermion densities, p-wave bosonic trimers could indeed be stabilized as the actual ground state in the system already for the typical experimental parameters.

V. DISCUSSION AND OUTLOOK

In this paper, we have studied the influence of confinement and finite interaction ranges on the formation of ground-state trimers in confined three-body systems of two identical fermions interacting with a mobile quantum impurity. We have shown that the position of the dimer-to-trimer transition previously characterized in Refs. [23, 32, 33] varies significantly under these effects and that leveraging these effects can, in principle, lead to the observation of p-wave trimers in atomically-thin semiconductors and ultracold quantum gases. While in two-dimensional cold atom systems already a great variety of mass ratios is available, trimer formation could be further enhanced using trapping confinement. In TMDs, such mass ratios are not readily available (unless flat bands are considered). However, our results show that the finite exciton-electron interaction range along with
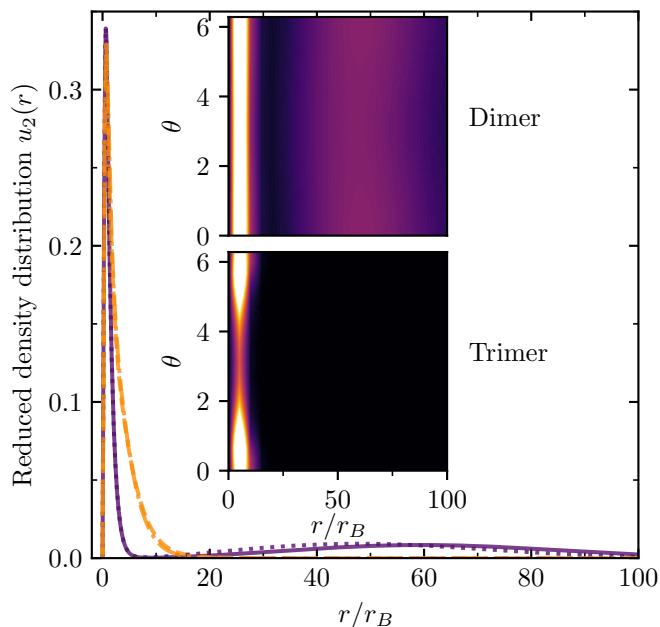
FIG. 7. Reduced density distributions of a dimer ($\alpha = 2$) and trimer ($\alpha = 3.5$) state with Coulomb interaction. The plot shows $u_2(r)$ for a dimer (purple, solid) and a trimer (orange, dashed) state for $R/r_B = 100$, $r_0/r_B = 0.8$ and $q = 0.3$ and a dimer (purple, dotted) and a trimer (orange, dash-dotted) state for $R/r_B = 100$, $r_0/r_B = 0.8$ and $q = 0.1$. The inset shows $u_1(r, \theta)$ for the trimer ($\alpha = 3.5$, lower) and the dimer state ($\alpha = 2$, upper) with $R/r_B = 100$, $r_0/r_B = 0.8$ and $q = 0.3$. The exponential decay and the delocalized tail, respectively, are visible and as before a slight tendency towards anti-parallel orientation of the fermions is present.

confinement enhance and stabilize trimer formation. Furthermore, we have argued that, given a suitable TMD, such trimers can, in principle, survive Coulomb repulsion as long as the effective charge, given by material parameters such as the dielectric constant, remains below a critical value.

In regards of the interpretation of confinement as a means to imitate finite bath density in many-body problems, the remarkable robustness of the dimer-trimer transition we find under moderate confinement, suggests that bosonic p-wave trimers might already appear as the ground state of typical TMD setups. Our work thus highlights that experiments may already now be close to the

point of exploring exciton-induced p-wave electron pairing, opening up the avenue to study novel mechanisms of boson mediated p-wave superconductivity in van-der Waals materials.

Moving forward from our work, there are several further exciting paths to pursue. For one, it has been shown that for systems with a greater number of bath particles also higher-order bound states may play an important role, which could outcompete the trimer state. The influence of confinement and finite range on these states is unexplored and might drastically change the position of ground state transitions as well as the occurrence of these transitions in the first place. Furthermore, moving beyond $1 + N$ type systems, the phase diagram of Bose-Fermi mixtures at a given density imbalance of the constituent species might be studied in few-body systems with comparable density ratios. In this regard, the occurrence, nature, and dynamics of interesting phenomena such as phase separation in the many-body regime could be illuminated by corresponding observations in a few-body system. For example, in a system of type $2+3$, one might compare the formation of a four or five-particle bound state to the coexistence of a dimer with a trimer.

In this pursuit, cold atom systems offer a wealth of tunable parameters such as mass ratio, bound state energy and confinement. Coulomb repulsion in turn may find an analogue in the repulsion between dipolar molecules, highlighting the possibility of cold atom systems as a platform to gain new insights into the physics of the exciton-electron mixtures in two-dimensional van der Waals materials.

[1] L. N. Cooper, Bound electron pairs in a degenerate fermi gas, Phys. Rev. **104**, 1189 (1956).

[2] J. Bardeen, L. N. Cooper, and J. R. Schrieffer, Theory of superconductivity, Phys. Rev. **108**, 1175 (1957).

[3] J. B. Ketterson and S. N. Song, *Superconductivity* (Cambridge University Press, 1999).

[4] D. J. Scalapino, A common thread: The pairing interaction for unconventional superconductors, Rev. Mod. Phys. **84**, 1383 (2012).

[5] A. Mackenzie and Y. Maeno, p-wave superconductivity, Physica B: Condensed Matter **280**, 148 (2000).

[6] O. Viyuela, L. Fu, and M. A. Martin-Delgado, Chiral topological superconductors enhanced by long-range interactions, Phys. Rev. Lett. **120**, 017001 (2018).

[7] J. R. Kirtley, C. C. Tsuei, J. Z. Sun, C. C. Chi, L. S. Yu-Jahnes, A. Gupta, M. Rupp, and M. B. Ketchen, Symme-

try of the order parameter in the high-tc superconductor YBa2cu3o7- δ, Nature **373**, 225 (1995).

[8] S. A. Kivelson, V. J. Emery, and H. Q. Lin, Doped antiferromagnets in the weak-hopping limit, Phys. Rev. B **42**, 6523 (1990).

[9] S.-K. Jian, Y. Huang, and H. Yao, Charge-4e superconductivity from nematic superconductors in two and three dimensions, Phys. Rev. Lett. **127**, 227001 (2021).

[10] B. Uchoa and A. H. Castro Neto, Superconducting states of pure and doped graphene, Phys. Rev. Lett. **98**, 146801 (2007).

[11] R. Nandkishore, L. S. Levitov, and A. V. Chubukov, Chiral superconductivity from repulsive interactions in doped graphene, Nat. Phys. **8**, 158 (2012).

[12] B. W. H. Baugher, H. O. H. Churchill, Y. Yang, and P. Jarillo-Herrero, Optoelectronic devices based on electrically tunable p–n diodes in a monolayer dichalcogenide, Nat. Nano. **9**, 262 (2014).

[13] J. C. Wheatley, Experimental properties of superfluid ^{3}He, Rev. Mod. Phys. **47**, 415 (1975).

[14] A. J. Leggett, A theoretical description of the new phases of liquid ^{3}He, Rev. Mod. Phys. **47**, 331 (1975).

[15] D. Vollhardt and P. Wolfle, The superfluid phases of helium 3 (1990).

[16] G. R. Stewart, Unconventional superconductivity, Advances in Physics **66**, 75 (2017).

[17] D. S. Petrov, Three-body problem in fermi gases with short-range interparticle interaction, Phys. Rev. A **67**, 010703 (2003).

[18] V. Efimov, Energy levels of three resonantly interacting particles, Nucl. Phys. A **210**, 157 (1973).

[19] O. I. Kartavtsev and A. V. Malykh, Low-energy three-body dynamics in binary quantum gases, J Phys. B **40**, 1429 (2007).

[20] S. Giorgini, L. P. Pitaevskii, and S. Stringari, Theory of ultracold atomic fermi gases, Rev. Mod. Phys. **80**, 1215 (2008).

[21] J. Levinsen, T. G. Tiecke, J. T. M. Walraven, and D. S. Petrov, Atom-dimer scattering and long-lived trimers in fermionic mixtures, Phys. Rev. Lett. **103**, 153202 (2009).

[22] Y. Castin, C. Mora, and L. Pricoupenko, Four-body efimov effect for three fermions and a lighter particle, Phys. Rev. Lett. **105**, 223201 (2010).

[23] L. Pricoupenko and P. Pedri, Universal (1 + 2)-body bound states in planar atomic waveguides, Phys. Rev. A **82**, 033625 (2010).

[24] D. Blume, Universal four-body states in heavy-light mixtures with a positive scattering length, Phys. Rev. Lett. **109**, 230404 (2012).

[25] P. Massignan, M. Zaccanti, and G. M. Bruun, Polarons, dressed molecules and itinerant ferromagnetism in ultracold fermi gases, Rep. Prog. Phys. **77**, 034401 (2014).

[26] J. Levinsen and M. M. Parish, Strongly interacting two-dimensional fermi gases, Annu. Rev. Cold At. Mol. **3**, 1 (2015).

[27] B. Bazak and D. S. Petrov, Five-body efimov effect and universal pentamer in fermionic mixtures, Phys. Rev. Lett. **118**, 083002 (2017).

[28] B. Bazak and D. S. Petrov, Stable p-wave resonant two-dimensional fermi-bose dimers, Phys. Rev. Lett. **121**, 263001 (2018).

[29] A. Schirotzek, C.-H. Wu, A. Sommer, and M. W. Zwierlein, Observation of fermi polarons in a tunable fermi liquid of ultracold atoms, Phys. Rev. Lett. **102**, 230402 (2009).

[30] C. Kohstall, M. Zaccanti, M. Jag, A. Trenkwalder, P. Massignan, G. M. Bruun, F. Schreck, and R. Grimm, Metastability and coherence of repulsive polarons in a strongly interacting Fermi mixture, Nature **485**, 615 (2012).

[31] M. Cetina, M. Jag, R. S. Lous, I. Fritsche, J. T. M. Walraven, R. Grimm, J. Levinsen, M. M. Parish, R. Schmidt, M. Knap, and E. Demler, Ultrafast many-body interferometry of impurities coupled to a Fermi sea, Science **354**, 96 (2016).

[32] J. Levinsen and M. M. Parish, Bound states in a quasi-two-dimensional fermi gas, Phys. Rev. Lett. **110**, 055304 (2013).

[33] R. Liu, C. Peng, and X. Cui, Universal tetramer and pentamer bound states in two-dimensional fermionic mixtures, Phys. Rev. Lett. **129**, 073401 (2022).

[34] M. Sidler, P. Back, O. Cotlet, A. Srivastava, T. Fink, M. Kroner, E. Demler, and A. Imamoglu, Fermi polaron-polaritons in charge-tunable atomically thin semiconductors, Nat. Phys. **13**, 255 (2017).

[35] G. Wang, A. Chernikov, M. M. Glazov, T. F. Heinz, X. Marie, T. Amand, and B. Urbaszek, Colloquium: Excitons in atomically thin transition metal dichalcogenides, Rev. Mod. Phys. **90**, 021001 (2018).

[36] Y. Shimazaki, C. Kuhlenkamp, I. Schwartz, T. Smoleński, K. Watanabe, T. Taniguchi, M. Kroner, R. Schmidt, M. Knap, and A. m. c. Imamoğlu, Optical signatures of periodic charge distribution in a mott-like correlated insulator state, Phys. Rev. X **11**, 021027 (2021).

[37] I. Amelio, N. Drummond, E. Demler, R. Schmidt, and A. Imamoglu, Polaron spectroscopy of a bilayer excitonic insulator, arXiv:2210.03658 (2022).

[38] A. Popert, Y. Shimazaki, M. Kroner, K. Watanabe, T. Taniguchi, A. Imamoğlu, and T. Smoleński, Optical sensing of fractional quantum hall effect in graphene, Nano Letters **22**, 7363 (2022).

[39] T. Smoleński, P. E. Dolgirev, C. Kuhlenkamp, A. Popert, Y. Shimazaki, P. Back, X. Lu, M. Kroner, K. Watanabe, T. Taniguchi, I. Esterlis, E. Demler, and A. Imamoğlu, Signatures of Wigner crystal of electrons in a monolayer semiconductor, Nature **595**, 53 (2021).

[40] Y. Zhou, J. Sung, E. Brutschea, I. Esterlis, Y. Wang, G. Scuri, R. J. Gelly, H. Heo, T. Taniguchi, K. Watanabe, G. Zaránd, M. D. Lukin, P. Kim, E. Demler, and H. Park, Bilayer Wigner crystals in a transition metal dichalcogenide heterostructure, Nature **595**, 48 (2021).

[41] J. von Milczewski, F. Rose, and R. Schmidt, Functional-renormalization-group approach to strongly coupled bose-fermi mixtures in two dimensions, Phys. Rev. A **105**, 013317 (2022).

[42] A. Imamoglu, O. Cotlet, and R. Schmidt, Exciton–polarons in two-dimensional semiconductors and the tavis–cummings model, Comptes Rendus. Physique **22**, 1 (2021).

[43] F. P. Laussy, A. V. Kavokin, and I. A. Shelykh, Exciton-polariton mediated superconductivity, Phys. Rev. Lett. **104**, 106402 (2010).

[44] O. Cotleţ, S. Zeytinoğlu, M. Sigrist, E. Demler, and A. m. c. Imamoğlu, Superconductivity and other collective phenomena in a hybrid bose-fermi mixture formed by a polariton condensate and an electron system in two dimensions, Phys. Rev. B **93**, 054510 (2016).

[45] J. J. Kinnunen, Z. Wu, and G. M. Bruun, Induced *p*-wave pairing in bose-fermi mixtures, Phys. Rev. Lett. **121**, 253402 (2018).

[46] C. Fey, P. Schmelcher, A. Imamoglu, and R. Schmidt, Theory of exciton-electron scattering in atomically thin semiconductors, Phys. Rev. B **101**, 195417 (2020).

[47] I. Bloch, J. Dalibard, and W. Zwerger, Many-body physics with ultracold gases, Rev. Mod. Phys. **80**, 885 (2008).

[48] N. Navon, R. P. Smith, and Z. Hadzibabic, Quantum gases in optical boxes, Nat. Phys. **17**, 1334 (2021).

[49] Y. Xu, X. Wang, W. L. Zhang, F. Lv, and S. Guo, Recent progress in two-dimensional inorganic quantum dots, Chem. Soc. Rev. **47**, 586 (2018).

[50] L. Bayha, M. Holten, R. Klemt, K. Subramanian, J. Bjerlin, S. M. Reimann, G. M. Bruun, P. M. Preiss, and S. Jochim, Observing the emergence of a quantum phase transition shell by shell, Nature **587**, 583 (2020).

[51] M. Holten, L. Bayha, K. Subramanian, C. Heintze, P. M. Preiss, and S. Jochim, Observation of pauli crystals, Phys. Rev. Lett. **126**, 020401 (2021).

[52] M. Holten, L. Bayha, K. Subramanian, S. Brandstetter, C. Heintze, P. Lunt, P. M. Preiss, and S. Jochim, Observation of cooper pairs in a mesoscopic two-dimensional fermi gas, Nature **606**, 287 (2022).

[53] A. Schirotzek, C.-H. Wu, A. Sommer, and M. W. Zwierlein, Observation of fermi polarons in a tunable fermi liquid of ultracold atoms, Phys. Rev. Lett. **102**, 230402 (2009).

[54] M. Koschorreck, D. Pertot, E. Vogt, B. Fröhlich, M. Feld, and M. Köhl, Attractive and repulsive fermi polarons in two dimensions, Nature **485**, 619 (2012).

[55] G. Ness, C. Shkedrov, Y. Florshaim, O. K. Diessel, J. von Milczewski, R. Schmidt, and Y. Sagi, Observation of a Smooth Polaron-Molecule Transition in a Degenerate Fermi Gas, Phys. Rev. X **10**, 041019 (2020).

[56] I. Fritsche, C. Baroni, E. Dobler, E. Kirilov, B. Huang, R. Grimm, G. M. Bruun, and P. Massignan, Stability and breakdown of Fermi polarons in a strongly interacting Fermi-Bose mixture, Phys. Rev. A **103**, 053314 (2021).

[57] In practice, this is achieved by setting $V_{\text{conf}}(\mathbf{r})/E_{\text{ref}} = (\mathbf{r}/R)^p$ where R is the box size, E_{ref} is a reference energy scale and p is a large integer so that an infinite potential well is approximated. In our calculation, we set $p = 30$ and use the vacuum dimer energy as the reference energy $E_{\text{ref}} = E_{2B}^{\infty}$.

[58] N. S. Rytova, The screened potential of a point charge in a thin film, MSU Phys. Bulletin **3**, 18 (1967).

[59] L. V. Keldysh, Coulomb interaction in thin semiconductor and semimetal films, JETP Lett. **29**, 658 (1979).

[60] M. Suzuki, Y. Suzuki, and K. Varga, *Stochastic Variational Approach to Quantum-Mechanical Few-Body Problems*, Vol. 54 (Springer Science & Business Media, 1998).

[61] J. Mitroy, S. Bubin, W. Horiuchi, Y. Suzuki, L. Adamowicz, W. Cencek, K. Szalewicz, J. Komasa, D. Blume, and K. Varga, Theory and application of explicitly correlated gaussians, Rev. Mod. Phys. **85**, 693 (2013).

[62] K. Varga, Solution of few-body problems with the stochastic variational method ii: Two-dimensional systems, Comp. Phys. Comm. **179**, 591 (2008).

[63] Y. Cho, S. M. Greene, and T. C. Berkelbach, Simulations of trions and biexcitons in layered hybrid organic-inorganic lead halide perovskites, Phys. Rev. Lett. **126**, 216402 (2021).

[64] J. Yan and K. Varga, Excited-state trions in two-dimensional materials, Phys. Rev. B **101**, 235435 (2020).

[65] M. Van der Donck, M. Zarenia, and F. M. Peeters, Excitons, trions, and biexcitons in transition-metal dichalcogenides: Magnetic-field dependence, Phys. Rev. B **97**, 195408 (2018).

[66] D. W. Kidd, D. K. Zhang, and K. Varga, Binding energies and structures of two-dimensional excitonic complexes in transition metal dichalcogenides, Phys. Rev. B **93**, 125423 (2016).

[67] As long as the size of the impurity-fermion bound state is smaller than the confinement length scale.

[68] S. K. Adhikari, Quantum scattering in two dimensions, American Journal of Physics **54**, 362 (1986).

[69] S. Becker, A. Michelangeli, and A. Ottolini, Spectral analysis of the 2+1 fermionic trimer with contact interactions, Math. Phys. Anal. Geom. **21**, 35 (2018).

[70] The $q = 0.5$, $R/r_B = 100$ data set shown in Fig. 6 does not show a trimer state, however this is merely due to the chosen plot range. A trimer state appears eventually upon increasing the mass ratio.

[71] Such a modification of the dielectric environment will also affect the trion binding energy resulting in a redefinition of E_{2B}^{∞}.

Appendix A: DETAILED DESCRIPTION OF THE SVM ALGORITHM

In this appendix, we seek to provide more information on the optimization process undertaken in every step of the SVM. For the results shown in the main text, we perform 10 independent calculations for every data point. In each of these calculations 100 basis states are found. In the following, we refer to each one of these calculations as a run and the combination of 10 runs makes up a single data point.

To compile a list of 100 basis states $\{\Phi_n\}_{n=1}^{100}$ in a single run, we successively increase the list of basis states by drawing from the manifold of trial wavefunctions described in the main text. In a step $N \to N+1$, we draw proposal states $\{\Phi_\alpha\}$ independently. From these proposals, we choose the state Φ_β which produces the lowest-lying eigenstate of the Hamiltonian H with respect to the vector space V_α^N spanned by the states $\{\Phi_n\}_{n=1}^N \cup \Phi_\alpha$. Specifically,

$$V_\alpha^N = \text{span}\left(\{\Phi_n\}_{n=1}^N \cup \Phi_\alpha\right) \qquad (A1)$$

$$\{\lambda_{\alpha,1}^N, ..., \lambda_{\alpha,N}^N\} = \sigma(H|_{V_\alpha^N}) \qquad (A2)$$

$$\beta = \min_\alpha \left[\min_i (\{\lambda_{\alpha,i}^N\}_i) \right], \qquad (A3)$$

where $\sigma(H|_{V_\alpha^N})$ denotes the spectrum of the Hamiltonian H restricted to the vector space V_α^N and the minimization over i chooses the lowest eigenvalue of $H|_{V_\alpha^N}$, while the minimization over α optimizes the proposal state.

Next, we perform a random descent walk in the vicinity of Φ_β, for which every step is accepted so long as it lowers the lowest eigenvalue.

A straight-forward method to draw independently from the ECG manifold is to draw proposal states Φ_α as

$$m_\alpha = \frac{1}{R} \begin{pmatrix} x_{11} & x_{12} & x_{13} \\ x_{21} & x_{22} & x_{23} \\ x_{31} & x_{32} & x_{33} \end{pmatrix} \qquad (A4)$$

with

$$A_\alpha = m_\alpha^T m_\alpha \qquad (A5)$$

where the x_{ij} are drawn from a uniform distribution in the interval $x_{ij} \in [-1, 1]$. The corresponding (unrenormalized) basis state is then given as $\Phi_\alpha(\mathbf{r}_1, \mathbf{r}_2, \mathbf{r}_3) = \mathcal{P} \exp\left(-\frac{1}{2} \sum_{i,j=1}^{3} A_{\alpha,ij} \mathbf{r}_i \cdot \mathbf{r}_j\right)$. In the second part of the optimization, we then update the proposal as

$$m'_\beta = m_\beta + \delta x \begin{pmatrix} x_{11} & x_{12} & x_{13} \\ x_{21} & x_{22} & x_{23} \\ x_{31} & x_{32} & x_{33} \end{pmatrix} \qquad (A6)$$

with

$$A'_\beta = (m'_\beta)^T m'_\beta, \qquad (A7)$$

where a value of $\delta x = 1$ has shown to yield good results.

As the manifold of trial functions is fairly large, a large number of such random proposals is necessary in every step of the algorithm to ensure convergence. While this choice of sampling quickly yields reliable results for molecule states, for trimer states convergence is much slower and especially close to the molecule-trimer transition, it can occur that no trimer state is obtained. To reduce the number of required steps and improve stability of the algorithm, we leverage the physical intuition, that a trimer state should feature all the particle confined within a length scale of the interaction range from each other. As the matrices A_α^{-1} carry the meaning of a covariance matrix, this thus suggests a covariance matrix of close to constant value (proportional to the mean distance squared of the particles from the center of the trap) with fluctuations around this value of the order of the interaction range. We thus introduce a further sampling method described as

$$B = 5Rx_0 + 2r_0 \begin{pmatrix} x_{11} & x_{12} & x_{13} \\ x_{21} & x_{22} & x_{23} \\ x_{31} & x_{32} & x_{33} \end{pmatrix},$$
$$A_\alpha^{-1} = \frac{B + B^T}{2}, \qquad (A8)$$

where $x_0 \in [0, 1]$, $x_{i,j} \in [-1, 1]$ and the corresponding random walk method is given by

$$B' = B + dx \begin{pmatrix} x_{11} & x_{12} & x_{13} \\ x_{21} & x_{22} & x_{23} \\ x_{31} & x_{32} & x_{33} \end{pmatrix},$$
$$(A'_\alpha)^{-1} = \frac{B' + (B')^T}{2}. \qquad (A9)$$

Here, the value of $5R$ as a sampling range for the mean distance squared of the particle from the center of the trap was chosen, because it ensured reasonably convergence. The range of $2r_0$ for the interparticle distances was picked due to the physical picture that the confinement of particles to the each other should be on the order of the interaction range. We thus alternate between these two sampling methods in the optimization procedure.

While especially the latter sampling method is very biased, we would like to highlight that these type of states are usually also found using the former sampling method, however many more sampling steps are necessary for this. Furthermore, due to the large number of sampling steps, about 15 thousand independent samples and 15 thousand local descents, repeated twenty times for every run, the exact form of the sampling coefficients used in Eqs. (A4) and (A9) plays a less dominant role.

After we have performed 10 different runs, each yielding 100 basis states, we then combine the results of these different runs to obtain a basis set of 1000 basis states $\{\Phi_n\}_{n=1}^{1000}$. Finally, the Hamiltonian is diagonalized with respect to these 1000 states and the physical quantities are extracted from the resulting ground-state. These results are shown in the main text.

Appendix B: EXACT SOLUTION OF THE TWO-BODY PROBLEM

We consider an impurity (with mass m_I) interacting with a single fermion (with mass m_F) via $V_{\mathrm{FI}}(\mathbf{r}) = -V_0\theta(r_0 - |\mathbf{r}|)$ where $\theta(x)$ is Heaviside function. The Schroedinger equation in the relative coordinate reads

$$-\frac{\nabla^2}{2\mu}\psi(\mathbf{r}) + V_{\mathrm{FI}}(\mathbf{r})\psi(\mathbf{r}) = E_{2B}^\infty \psi(\mathbf{r}) \qquad (B1)$$

where $\mu = m_F m_I/(m_F + m_I)$ is the reduced mass of impurity and fermion. Notice that the wavefunction $\psi(\mathbf{r})$ can be decomposed into a radial part and an angular part, i.e. $\psi(\mathbf{r}) = u(r)e^{im\theta}$ with m the angular momentum of the state. For the ground state we have $m = 0$, thus the equation for the radial wavefunction is

$$r^2 u'' + r u' + 2\mu[E_{2B}^\infty + V_0\theta(r_0 - r)]r^2 u = 0. \qquad (B2)$$

This equation can be solved analytically and the ground state energy E_{2B}^∞ satisfies

$$\sqrt{-2\mu E_{2B}^\infty}\,J_0\left(\sqrt{2\mu(E_{2B}^\infty+V_0)}r_0\right)K_1\left(\sqrt{-2\mu E_{2B}^\infty}r_0\right)-\sqrt{2\mu(E_{2B}^\infty+V_0)}K_0\left(\sqrt{-2\mu E_{2B}^\infty}r_0\right)J_1\left(\sqrt{2\mu(E_{2B}^\infty+V_0)}r_0\right)$$
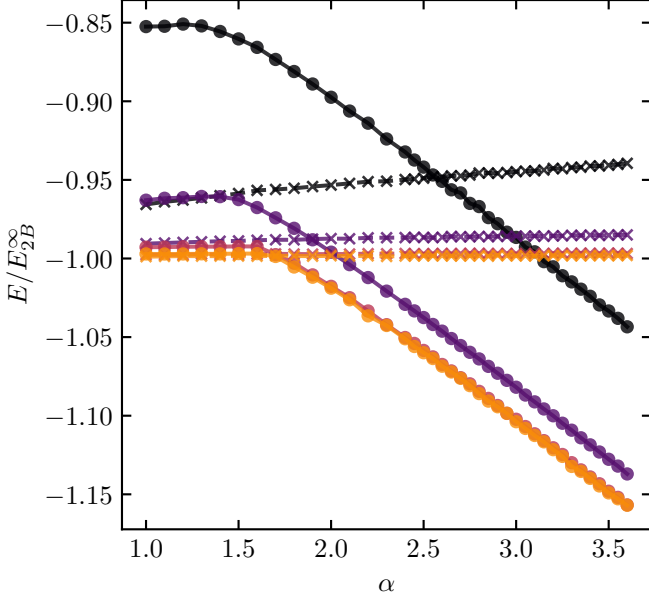$$=0$$

$$(B3)$$

FIG. 8. 3-body ground state energy (dots, solid lines) and 2-body ground state energy (crosses, dashed lines) with $r_0/r_B = 1.2$ and $R/r_B = 10$ (black), 20 (purple), 50 (red) and 100 (orange). The 2-body ground state energy increase linearly with mass ratio α, which coincide with the behavior of the 3-body ground state energy below the critical mass ratio.

with J_0, J_1 Bessel functions of the first kind and K_0, K_1 modified Bessel functions of the second kind.

Appendix C: TWO-BODY PROBLEM IN CONFINEMENT

In this appendix, we study the influence of confinement on the solution of the two-body problem presented in Appendix B. As such, we consider a two-body system consisting of one impurity (with mass m_I) and one fermion (with mass m_F) in a 2D spherical box. The Hamiltonian

then reads

$$H = -\frac{\hbar^2}{2m_I}\nabla_1^2 - \frac{\hbar^2}{2m_F}\nabla_2^2 + \sum_{i=1}^2 V_{\mathrm{conf}}(\mathbf{r}_i) + V_{\mathrm{FI}}(\mathbf{r}_1-\mathbf{r}_2),$$

$$(C1)$$

where we have used the same notation as in Appendix B and employed the SVM described in the main text to solve the problem.

In Fig. 8, we show the two-body ground state energy as well as the three body ground state energy for $r_0/r_B = 1.2$ and different values of R as a function of α. The vacuum dimer energies lie slightly higher than $-E_{2B}^\infty$ due to the confinement, while for larger system sizes the energies approach $-E_{2B}^\infty$. Additionally, a close to linear increase of the energies with mass ratio α is visible which decreases as R increases. This observation is well in-line with an interpretation of as the two body confinement energy $E_{\mathrm{conf}} = z_{01}^2/2m_I R^2 + z_{01}^2/2m_F R^2 = z_{01}^2(\alpha+1)/2m_F R^2$ where z_{01} is the first zero of Bessel function J_0. Comparing the three-body energy with the two-body energy, we can see that the three body energy below the critical mass ratio also increases linearly with α and the increase is larger for smaller box size. Additionally, especially for smaller system sizes the three-body energies below the critical mass ratio lie considerably higher than their two-body counterparts due to the confinement energy of the fermion in a scattering state as expected from our analysis in section IV A.

Appendix D: ANGULAR MOMENTUM

The total angular momentum of the $(2+1)$ system in the relative coordinate is given by $\mathbf{L}_{\mathrm{tot}} = \mathbf{L}_2 + \mathbf{L}_3 = \mathbf{R}_2 \times \mathbf{P}_2 + \mathbf{R}_3 \times \mathbf{P}_3$, where $\mathbf{R}_2$, $\mathbf{R}_3$, $\mathbf{P}_2$, $\mathbf{P}_3$ are the position and momentum of the two fermions in relative coordinate. Because our variational wavefunctions are always real functions, the expectation value of $\mathbf{L}_{\mathrm{tot}}$ with the wavefunction must vanish. In fact, $\langle \mathbf{L}_{\mathrm{tot}}\rangle = -i(\langle\mathbf{R}_2 \times \nabla_{\mathbf{R}_2}\rangle + \langle\mathbf{R}_3 \times \nabla_{\mathbf{R}_3}\rangle) = ir$ where r is a real number. On the other hand, $\langle \mathbf{L}_{\mathrm{tot}}\rangle$ is real because $\mathbf{L}_{\mathrm{tot}}$ is a hermitian operator. Therefore, we have $\langle \mathbf{L}_{\mathrm{tot}}\rangle = 0$.

In order to capture the transition from the dimer state (with $\langle\mathbf{L}_{\mathrm{tot}}\rangle = 0$) to the trimer state (with $\langle\mathbf{L}_{\mathrm{tot}}\rangle = \pm 1$), we calculate the expectation value of $\mathbf{L}_{\mathrm{tot}}^2$ instead. Given two gaussian functions $|A\rangle$ and $|B\rangle$, one can prove that the matrix element of $\mathbf{L}_{\mathrm{tot}}^2$ is

$$\langle A|\mathbf{L}_{\text{tot}}^2|B\rangle = \frac{8\pi^3}{\sqrt{\det{(A+B)}}}(\text{Tr}(f_1(A)(A+B)^{-1})\text{Tr}(f_1(B)(A+B)^{-1})/4 + \text{Tr}(f_1(A)(A+B)^{-1}f_1(B)(A+B)^{-1})/2$$
$$+ \text{Tr}(f_2(A)(A+B)^{-1})\text{Tr}(f_2(B)(A+B)^{-1})/4 + \text{Tr}(f_2(A)(A+B)^{-1}f_2(B)(A+B)^{-1})/2$$
$$+ \text{Tr}(f_1(A)(A+B)^{-1})\text{Tr}(f_2(B)(A+B)^{-1})/2 + \text{Tr}(f_1(A)(A+B)^{-1}f_2(B)(A+B)^{-1})).$$
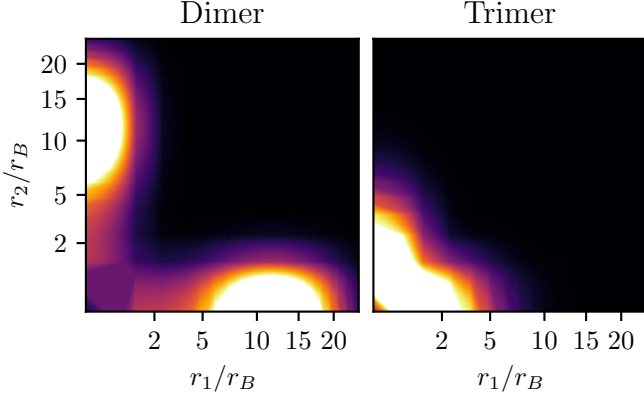$$\text{(D1)}$$

FIG. 9. Reduced density distribution $u_3(r_1, r_2)$ for a dimer ($\alpha = 2$, left) and a trimer ($\alpha = 3$, right) state for $r_0/r_B = 0.8$ and $R/r_B = 20$. For the trimer state, $u_3(r_1, r_2)$ attains its largest values when r_1 and r_2 are both small, which shows that both fermions are close to the impurity, while the dimer state $u(r_1, r_2)$ achieves its maximum on the x- and y-axis.

The functions $f_1(A)$ and $f_2(A)$ are defined in the following way. Given a 6×6 symmetric matrix A, it can always be expressed as

$$A = \begin{bmatrix} A_{11} & A_{12} & A_{13} \\ A_{12}^{\text{T}} & A_{22} & A_{23} \\ A_{13}^{\text{T}} & A_{23}^{\text{T}} & A_{33} \end{bmatrix}, \quad \text{(D2)}$$

where A_{ij} ($i \le j$) are 2×2 matrices. Let $R = \begin{bmatrix} 0 & 1 \\ -1 & 0 \end{bmatrix}$, $f_1(A)$ and $f_2(A)$ then read

$$f_1(A) = \begin{bmatrix} 0 & -A_{12}R & 0 \\ A_{12}^{\text{T}}R & 0 & A_{23}R \\ 0 & -A_{23}^{\text{T}}R & 0 \end{bmatrix}, \quad \text{(D3)}$$

$$f_2(A) = \begin{bmatrix} 0 & 0 & -A_{13}R \\ 0 & 0 & -A_{23}R \\ A_{13}^{\text{T}}R & A_{23}^{\text{T}}R & 0 \end{bmatrix}. \quad \text{(D4)}$$

Appendix E: REDUCED DENSITY DISTRIBUTION WITH r_1 AND r_2

To further study the anatomy of the dimer and trimer states with respect to their radial distribution, we define

the reduced density distribution $u_3(r_1, r_2)$ as

$$u_3(r_1, r_2) = \int |\Psi(\mathbf{r}, \mathbf{r} + \mathbf{r}_1, \mathbf{r} + \mathbf{r}_2)|^2 d^2\mathbf{r}d\theta_1 d\theta_2, \quad \text{(E1)}$$

where the vector $\mathbf{r}_1$ and $\mathbf{r}_2$ are parametrized as $\mathbf{r}_1 = (r_1 \cos\theta_1, r_1 \sin\theta_1)$, $\mathbf{r}_2 = (r_2 \cos\theta_2, r_2 \sin\theta_2)$. This function measures the probability of simultaneously finding one electron at the distance r_1 and another electron at distance r_2 from the impurity. In Fig. 9, we show the density distribution for a dimer and a trimer state. For the dimer state, the density distribution u_3 almost vanishes along the diagonal and achieves its maximum at approximately $(r_1/r_B, r_2/r_B) \approx (0, 12)$ because one fermion is closely bound to the impurity while another fermion is more delocalized. For the trimer state, u_3 attains its largest values when r_1 and r_2 are both close to 0 and vanishes rapidly for larger r_1 and r_2, which shows that both fermions are tightly bound to the impurity.

Appendix F: COULOMB INTERACTION

The Coulomb interaction between two charged particles is $V_C(\mathbf{r}) = \frac{q^2}{r}$, where we set the Coulomb constant $k = 1$ and the particles have equal charge q. We use the fact that for any potential $V(\mathbf{r})$

$$\langle A|V(\mathbf{r}_2 - \mathbf{r}_3)|B\rangle =$$
$$\frac{8\pi^3}{\sqrt{\det{(A+B)}}}\frac{a}{2\pi}\int V(r)\exp(-ar^2/2)d^2\mathbf{r}$$
$$\text{(F1)}$$

with $a = 1/((A+B)_{22}^{-1} + (A+B)_{33}^{-1} - 2(A+B)_{23}^{-1})$. The matrix element of the Coulomb potential between the two fermions is then

$$\langle A|V_C(\mathbf{r}_2 - \mathbf{r}_3)|B\rangle = q^2 \frac{8\pi^3}{\sqrt{\det{(A+B)}}}\sqrt{\frac{\pi a}{2}}. \quad \text{(F2)}$$